Computational simulation of round thermal jets in an ambient cross flow using a large-scale hydrodynamic model

Malcangio, Daniela; Cuthbertson, Alan; Ben Meftah, Mouldi; Mossa, Michele

Published in:
Journal of Hydraulic Research

DOI:
10.1080/00221686.2019.1684392

Publication date:
2019

Document Version
Peer reviewed version

Computational simulation of round thermal jets in an ambient cross flow using a large-scale hydrodynamic model

DANIELA MALCANGIO, Assistant Professor, *Department of Civil, Environmental, Land, Building Engineering and Chemistry, Polytechnic University of Bari, Bari, Italy*

Email: daniela.malcangio@poliba.it (author for correspondence)

ALAN CUTHBERTSON (IAHR Member), Senior Lecturer, *School of Science and Engineering, University of Dundee, Dundee, UK*

Email: a.j.s.cuthbertson@dundee.ac.uk

MOULDI BEN MEFTAH, Assistant Professor, *Department of Civil, Environmental, Land, Building Engineering and Chemistry, Polytechnic University of Bari, Bari, Italy*

Email: mouldi.benmeftah@poliba.it

MICHELE MOSSA (IAHR Member), Full Professor, *Department of Civil, Environmental, Land, Building Engineering and Chemistry, Polytechnic University of Bari, Bari, Italy*

Email: michele.mossa@poliba.it

Running Head: Simulation of round thermal jets in ambient cross flows.

Computational simulation of round thermal jets in an ambient cross flow using a large-scale hydrodynamic model

ABSTRACT

This paper presents the numerical simulation of single, circular, turbulent, thermal jets discharged into an ambient fluid body with a uniform cross flow. The study utilizes a 3D hydrodynamic model to predict the dynamics of the evolving jets, with the model simulations calibrated against benchmark laboratory experimental datasets. Within the numerical-experimental model comparisons, the mean centreline temperature and velocity fields of the evolving jets are investigated in order to understand and predict the jet diffusion characteristics within the flowing ambient fluid body. Direct comparison between the numerical model predictions and laboratory datasets reveals that, with appropriate parameterization of the mixing processes and the selection of an appropriate numerical grid resolution, the large-scale hydrodynamic model can simulate both the near- and far- field thermal jet behavior with good overall agreement, thus revealing a valid modelling tool used by environmental regulators for assessing the conformity of water quality of marine wastewater discharges.

Keywords: Dispersion processes and models; laboratory studies; numerical simulations; RANS models; turbulent jets; velocity and temperature measurements.

1 Introduction

Nowadays, one of the principal aims of studying the behavior of jets and plumes, whatever their type (i.e. pure jets, thermal plumes or buoyant jets), is to mitigate their environmental impact within the ambient fluid bodies into which they are discharged. Within the marine environment, these discharges are normally considered to be polluting substances that can have significant detrimental impacts on the receiving waters (e.g. domestic and industrial wastewater, stormwater run-off, heated condenser water from thermal power stations and hydroelectric plants). Within the current study, we focus on the near-field mixing behavior of thermal jet discharges into flowing ambient water bodies, limiting our investigations to specific cases where buoyancy effects due to the temperature difference between the ambient fluid and the jet discharge can be regarded as minimal.

In this context, the mixing and dilution of pollutants within receiving water bodies constitutes a physical environmental problem that often needs rapid intervention in critical situations (e.g. during unplanned pollutant spills). Here, near-field numerical model predictions are therefore of crucial importance to mitigate potential environmental damage to the marine environment. A number of different numerical modelling approaches have been developed and utilized for this purpose. At the simplest level, general jet integral models were developed initially by considering the jet diffusion approach (Abraham, 1963) and applying a

jet entrainment closure term (Fan, 1967). These integral model approaches have been developed and adopted widely to predict time-averaged, near-field characteristics (e.g. trajectories, centerline velocities, concentrations and dilutions) of single round buoyant jets (Jirka, 2004) and plane buoyant jets (Jirka, 2006). Related studies adopting these integral modelling techniques have also focused on developing (i) different approaches to the required entrainment closure assumptions, (ii) alternative Eulerian or Lagrangian formulations (Lee and Vincent, 2003), and (iii) a greater consideration of the influence of ambient fluid conditions (i.e. density stratification and cross flows) (Jirka, 2004, 2006). As such, integral models are well-regarded as providing a reasonable representation of the jet or plume behavior under general flow conditions and form the underlying theoretical basis of many regulatory mixing zone models for marine wastewater discharges or atmospheric emissions, such as CORMIX (Doneker and Jirka, 2007).

In recent years, Computational Fluid Dynamics (CFD) methods have been applied increasingly as a simulation tool in engineering design for the analysis of turbulent flows, including jets and plumes (Sotiropulos, 2005). The theoretical basis of all CFD modelling techniques is the Navier-Stokes (N-S) equations. When these N-S equations are time averaged, the resulting numerical modelling approaches are commonly defined as Reynolds-Averaged Navier-Stokes (RANS) methods, which are used widely in many CFD applications in relation to the analysis of turbulent flows, where the main interest is to gain information about temporally-averaged flow behavior (Shahryar and Moshfegh, 2013; Arunajatesan, 2012; Hwang et al., 1995; Zeng and Huai, 2008; Yang et al., 2015). In the context of the current study, simple RANS models can predict laminar, transitional, and turbulent regions of a three-dimensional round jet, while their main advantage over Direct Numerical Simulation (DNS) of the Navier-Stokes equations is that DNS techniques require significantly greater computational resources that increase dramatically with flow Reynolds numbers (Gohil et al., 2011). Therefore, application of DNS techniques has mainly been restricted to the simulation of turbulent flows with relatively low Reynolds numbers. Large Eddy Simulation (LES) has also been proposed recently as an alternative technique to study the jet spreading and dilution within a flowing ambient environment (Ma et al., 2007; Guan and Wu, 2007; Gao et al., 2018). While, in RANS models, the N-S equations are time averaged to transform them into a steady form, in LES, the N-S equations are filtered spatially in order to resolve motions larger than the computational grid size. Both RANS and LES approaches have their advantages and drawbacks in practical engineering situations. Specifically, LES models are extremely expensive and infeasible to utilize in routine engineering design as they require very high resolution computational meshes and very fine temporal discretization. In more specialized applications, however, they can provide a practical modelling tool for the study of turbulent flows at high spatio-temporal resolutions for engineering-relevant high Reynolds numbers,

which requires both high grid resolutions and high performance computing (Roberts et al., 2010). As a simpler, less computationally demanding approach, RANS models, if well calibrated, can provide good predictions of the mean behavior of jets and plumes (Tang et al., 2008).

Due to the complexity of the transport mechanisms, mixing characteristics and, ultimately, the fate of turbulent jets discharged into different water environments, a range of different modelling approach have typically been adopted, depending on the various phases of mixing and key factors controlling these mixing phases. Within near-field mixing zone models, the entrainment, mixing and dilution characteristics for turbulent jets are controlled primarily by the source discharge conditions. By contrast, mixing and dilution in far-field hydrodynamic models are controlled by environmental conditions in the ambient fluid body (e.g. currents, bathymetry, winds, density stratification, waves and tides). As such, the clear distinction between these two major model categories is well defined in literature (Roberts et al., 2010) and only a few previous studies have attempted to use large-scale hydrodynamic modelling approaches to predict turbulent jet behavior in the near-field mixing zone (Blumberger et al., 1996; Zhang and Adams, 1999).

In the current study, this alternative approach is utilized to simulate thermal turbulent jets in a cross-flowing ambient fluid, based on application of a commercially-available, large-scale circulation model. The numerical simulations are performed with the hydrodynamic model MIKE 3 (by DHI), which has been utilized previously for hindcasting and forecasting of various hydro-physical (e.g. hydrodynamic, water quality and sediment transport) modelling scenarios in natural water bodies and verified extensively by in situ measurements (Pietrzak et al., 2002; Lumborg, 2005; Lessin and Raudsepp, 2006; Malcangio and Petrillo, 2010; Mali et al., 2018; Malcangio et al., 2017). The novelty of the present work is in applying this large-scale model to predict both the near- and far- field hydrodynamic processes of turbulent jets in a cross-flowing ambient fluid body. These computational simulations are compared with experimental data collected at the Coastal Engineering Laboratory (LIC) of the Polytechnic University of Bari, Italy (Malcangio et al., 2008; Ben Meftah et al., 2014; Ben Meftah et al., 2015; Malcangio and Mossa, 2016; Malcangio et al., 2016; Ben Meftah et al., 2018), with the RANS model calibration and verification focusing on time averaged velocity and concentration fields from the LIC datasets. In general, the level of comparability between the numerical simulations and experimental data suggest that the numerical simulation tool MIKE 3 can be applied successfully to simulate the dynamics of turbulent jets in a cross-flow.

2 Experimental Scaling and Methods

2.1 Definition of problem

The problem under investigation concerns a vertical, round effluent jet discharged into a bounded ambient water body of total depth H and with a uniform cross-flow velocity U_a (see Fig. 1). This arrangement is defined in respect to a Cartesian coordinate system (x, y, z), where the x- and z-axis are positive in streamwise and vertical upward directions, respectively, while the y-axis represents the lateral, cross-channel direction. The origin of the coordinate system (0, 0, 0) aligns with the centerline of the jet source (in plan) at the elevation of the channel bottom (Fig. 1). As such, the jet is discharged vertically at the source location (0, 0, h_0) from a single round nozzle of internal diameter D and a mean exit velocity U_0. As the source density of the effluent, ρ_0, is lower than the ambient density, ρ_a [= ρ_0 + $(\Delta\rho)_0$], the effluent discharge is a positively buoyant jet. According to previous studies (Pratte and Baines, 1967; Rajaratnam, 1976; Andreopoulos and Rodi, 1984), turbulent buoyant jets can be characterized by their initial kinematic fluxes of volume Q, momentum M, and buoyancy B, such that

$$Q = \frac{\pi D^2}{4} U_0, \quad M = \frac{\pi D^2}{4} U_0^2 = Q U_0, \text{ and } \quad B = \frac{\pi D^2}{4} U_0 g_0' = g_0' Q \tag{1}$$

where g'_0 [= $g(\Delta\rho)_0/\rho_a$] is the modified gravitational acceleration at the source and g is the gravitational acceleration (g = 9.81 m s^{-2}). The upper surface of the receiving fluid body is free, and the solid bottom boundary of the system is flat and horizontal.

2.2 Definition of length scales

The behavior of a vertical turbulent buoyant jet discharged into a laterally unconfined body of ambient fluid can be parameterized fully by the densimetric Froude number F_0 [= $U_0/(g'_0 D)^{1/2}$] at the source and the velocity ratio $r = U_0/U_a$. However, close to the source, the vertical buoyant jet behavior either has jet-like or plume-like characteristics depending on the relative magnitudes of Q, M and B. Physical interpretation of the jet structure in this near-source region is further aided by the derivation (through dimensional analysis) of two characteristic length scales l_Q and l_M, such that

$$l_Q = Q_0 / M_0^{1/2}, \text{ and } \quad l_M = M_0^{3/4} / B_0^{1/2}, \tag{2}$$

where, l_Q [= $(\pi/4)^{1/2} D \approx D$] represents the initial transition length for a pure jet and l_M represents the transition length between jet-like and plume-like behavior, with the latter related to F_0 through l_M [= $(\pi/4)^{1/4} D(\mathsf{F}_0)$]. Two additional characteristic length scales that

include the influence of ambient cross-flow U_a can also be defined through dimensional analysis as

$$l_m = M_0^{1/2}/U_a, \text{ and } l_b = B_0/U_a^3 \quad (3)$$

Both l_m and l_b represent the vertical distance along the jet trajectory where the respective vertical velocities associated with the momentum-dominated (MD) jet and buoyancy-dominated (BD) plume decay to the order of the cross-flow velocity U_a (i.e. the approximate elevation at which the jet/plume is bent over by the cross-flow). These length scales l_M, l_m and l_b provide convenient estimates of the relative contributions of momentum, buoyancy and ambient flow advection in jet development (Fisher et al., 1979; Wright, 1977, 1984; Lee and Neville-Jones, 1987) and the relationship between them is useful to describe the trajectory and dilution characteristics (Wright, 1977, 1984), depending on whether the buoyant jet is in the MD or BD regime and whether the observation is in the near-field (NF) or far-field (FF). [Note, the trajectory of the buoyant jet is affected significantly by a bounded ambient flow when the empirical condition $H/l_b > O(1)$ is satisfied (Lee and Neville-Jones, 1987). This condition is designated conventionally as buoyancy-dominated far-field (BDFF) flow).

The dynamic influence of the ambient current is also determined by the effective velocity ratio

$$r_{eff} = [(\rho_0 U_0^2)/(\rho_a U_a^2)]^{1/2} = r\,(\rho_0/\rho_a)^{1/2} \quad (4)$$

This dimensionless parameter did not show a significant difference from the jet-to-cross flow velocity ratio, $r = U_0/U_a$, typically used for constant-density flows, as considered herein, that are simulated numerically and reproduced in laboratory experiments (Malcangio and Mossa, 2016).

In the analysis of buoyant jets, the centerline trajectory based on jet velocity is usually defined by the locus of the maximum velocity (or total pressure), while the trajectory based on maximum jet concentration or temperature is normally determined from concentration/temperature profiles or fields obtained by micro-CTD probes or flow visualization techniques (e.g. laser-induced fluorescence), respectively. Measurements of both trajectory types are reported in several past studies for vertical jets in cross-flows in the *xz*-plane of symmetry along the jet centreline (Rajaratnam, 1976; Wright, 1977; Priestly, 1956; Moore, 1966; Chu and Goldberg, 1974; Cuthbertson and Davies, 2008). To determine the buoyant jet trajectories within the current study, the experimental data and numerical predictions of temperature and velocity fields were utilised through tracking their maximum values in the evolving buoyant jet. These trajectories were compared with common empirical laws found in literature and scaled through different normalizations.

2.3 Experimental set-up

The experimental apparatus at LIC is composed of (i) a glass-walled, rectangular, recirculating water channel of length 15 m, width 4 m wide and depth 0.4 m, and (ii) the thermal-hydraulic buoyant jet injection system (Malcangio and Mossa, 2016). The receiving ambient water had a uniform freshwater density (ρ_a = 996 kg m^{-3} at T_a = 27 °C) with a constant depth H = 0.26 m. As the flow depth H is much smaller than the mean channel width, W, with a resulting flow aspect ratio W/H = 15.4 (i.e. >> 1), this set-up can be regarded as a shallow flow condition. As such, the channel side walls were assumed to have no effect on the buoyant jet development and mixing within the flowing ambient. The cross-flow velocity U_a was set at 0.089 m s^{-1}, meaning that the equivalent ambient flow Reynolds number $\mathsf{R}_e = 4U_aR_H/\nu$ (with ν = kinematic viscosity of the ambient fluid, R_H = channel hydraulic radius) was approximately 9.3×10^4 (i.e. fully turbulent flow). The thermal buoyant fluid at initial temperature $T_0 = T_a + (\Delta T)_0$ was pumped at a constant prescribed rate Q_0 through a vertically-aligned, round nozzle of diameter D = 5 mm at the centreline of the rectangular channel section and at an elevation h_0 = 40 mm above the flat, horizontal channel bottom (see Fig. 1). Details of the parametric conditions considered in the experimental tests are given in Table 1. In this regard, the parametric dependence of the thermal jet behavior was considered by varying (i) the temperature difference $(\Delta T)_0 = T_0 - T_a$, and (ii) the exit velocity of the jet $U_0 = 4Q_0/(\pi D^2)$ in the experimental tests. As previously indicated, this is fully accounted for dynamically by the densimetric Froude number F_0 [or the related jet Richardson number $\mathsf{R}_{i0} = (\pi/4)^{1/4}\,(g'_0\,D/U_0^2)^{1/2} = (\pi/4)^{1/4}\,(1/\mathsf{F}_0)$] and the jet-to-ambient velocity ratio r (see Table 1). In addition, the initial jet Reynolds number $\mathsf{R}_{e0} = 4Q_0/(\pi D\nu)$ was sufficiently high [i.e. O(10^4), Table 1] to consider the jets to be fully turbulent.

Following initial release of the jet, statistically-steady discharge conditions were typically achieved after about 10 minutes. At this point, the temperature and velocity field measurements were carried out. The channel was equipped with a *xyz* traversing system, allowing measurements to be taken in the three-dimensional planes (i.e. *xy*, *yz* and *xz*). Within the current study, measurements were obtained on the *xz*-plane of flow symmetry (i.e. along the jet centreline) at a spatial resolution of 1 cm intervals. Four resistance temperature detectors (RTD) were used to measure the temperature field. One RTD was installed on the traversing instrument support to measure the temperature T of the dispersed jet within the ambient cross-flow, one was sited in the upstream tank of the recirculating channel to measure the ambient water temperature T_a, one in the feed tank for fresh water supply and heating, and one in the head tank for the initial jet temperature T_0 measurements prior to discharge. The measurement zone of the RTDs is a 25 mm insert from the closed end (tip) of

the probe and the detectors can obtain 250 temperature measurements per second (i.e. a maximum data acquisition frequency of 250 Hz).

A down-looking Nortek Acoustic Doppler Velocimeter (ADV) probe system was used for the velocity measurements. At each measurement point in the flow field, the three components of instantaneous velocity (u, v, w) were acquired for 200 s at an acquisition frequency of 25 Hz (i.e. 5,000 instantaneous velocities per measurement location) with an estimated measurement error of ± 0.15 mm s^{-1}. The sampling volume of the down-looking ADV probe was located 5 cm below the transducers to minimize flow interference.

2.4 Flow solver and numerical method

The numerical model used in this study is the hydrodynamic simulation tool MIKE 3, developed by the Danish Hydraulic Institute (DHI). It is a professional engineering software package for three-dimensional free-surface flows, designed in a modular structure and applicable to simulations of hydraulics, water quality and sediment transport in water bodies (DHI Software, 2009). The suitability of this model has been tested in previous studies considering the planning of brine outfalls from desalination plants (Malcangio and Petrillo, 2010) and forced mixing systems in ports (Malcangio et al., 2017), both providing good results in the large-scale domain. This current study required the application of the hydrodynamic module (HD), which solves the continuity and momentum equations in three dimensions, applying the so-called RANS equations in a Cartesian coordinate system (x, y, z) (DHI Software, 2009). This model was applied in non-hydrostatic conditions and an artificial compressibility method (ACM) coupling directly the pressure and velocity fields was therefore used. It is well known that ACM provides an excellent tool to enforce a faster convergence in steady state simulations (DHI software, 2009), where the total pressure is decomposed into hydrostatic and hydrodynamic contributions. As such, the ACM was used for the hydrodynamic part, as opposed to the Poisson equation, which is commonly adopted in Navier-Stokes algorithms. This is possible only by adding a time derivative of pressure into the incompressible continuity equation, leading to a change in the governing equations from elliptic-parabolic to hyperbolic-parabolic equations (Lee et al., 2006).

The discharge of pollutants (e.g. thermal discharges from power stations) can be introduced into MIKE 3 model as a source or sink term at given locations and depths. More details on the configuration of sources and/or sinks in the numerical model have been previously reported by Malcangio and Petrillo (2010). Within the present study, the 3D HD model was coupled with the advection-dispersion (AD) model in order to calculate the spreading of thermal discharges in which horizontal and vertical density gradients result only from temperature variations between the discharge and the ambient fluid. The eddy diffusivity

of temperature is assumed to be proportional to the effective eddy viscosity, with a factor of proportionality $1/\sigma_T$, where σ_T being the Prandtl/Schmidt number. Values of σ_T greater than unity imply that diffusive transport is weaker for temperature than for fluid momentum. Two values of σ_T are considered, i.e. $\sigma_T = 1$ and 10 during model calibration and sensitivity analysis phase. These correspond to dispersion factors $1/\sigma_T = 1$ and 0.1, respectively. Calibration of the model to σ_T was performed only after the sensitivity of model predictions to grid resolution and the selected turbulence model had been conducted, and the most appropriate grid spatial resolution and turbulence model had been selected, as discussed in the following sections (3.1 and 3.2).

Among the possible advection-dispersion schemes, the 3D QUICKEST-SHARP was selected as it is especially suitable for numerical simulations with steep concentration (or temperature) gradients. The numerical algorithm and solution technique for this scheme is described in Vested et al. (1992). For the RANS calculations, the governing equations are mathematically time-independent, but numerically the equations are integrated over a pseudo time to update the velocity from an initial condition until it reaches the correct solution of time-independent RANS equations.

The model solves the equations for source volumetric, momentum and buoyancy, together with the conservation equation for the temperature, and with the equation of state of the ambient water relating the local density to temperature and pressure. The finite difference method, solved on a structured (rectangular) grid, was used along with the Courant-Friedrichs-Lewy stability condition, and in conjunction with appropriate initial and boundary conditions.

The flow field and pressure variation are computed by the mathematical model in response to a variety of forcing functions. For this study, the vertical velocity profile was assumed to be uniform over the whole two boundaries, with an average velocity value of 0.084 m s^{-1}. The jet discharge was represented by a source condition characterized by different initial water temperature excesses $(\Delta T)_0$ and jet nozzle flow rates Q_0. No additional information on the turbulent flow structure at the round jet orifice (e.g. mean velocity profile or turbulence intensities) was included in the boundary conditions, partly due to the lack of experimental measurements close to the source and partly due to the numerical grid resolution (i.e. Δx, $\Delta y = D/4 \rightarrow 2D$, see section 3.1).

Further details on the spatial resolution and the turbulence closure scheme are discussed in the following sections, as well as the comparison between experiments and measurements of tests summarized in Table 1.

3 Results and discussion

3.1 Grid sensitivity analysis

A review of previous investigations on the numerical study of turbulent round jets indicates that the computational grid discretization used can have a strong effect on the efficacy of the results. For example, Jones and McGuirk (1980) predicted larger mixing rates for a single round jet in a confined cross flow compared to the experimental data of Kamotani and Greber (1972); the discrepancy being attributed to numerical diffusion error caused by the course grid discretization and to the turbulence model utilized. Similarly, the computational simulations by Holdeman and Srinivasan (1984) of non-isothermal mixing in a confined cross flow indicated much lower mixing rates than corresponding experimental measurements, with a significant influence observed on the grid selection and the levels of numerical diffusion obtained in the solutions.

The discretization of the ambient open channel water body was investigated in depth in this study. The MIKE 3 software permits the adoption of a structured (rectangular) grid and allows the choice of a non-hydrostatic engine, applying the artificial compressibility method (ACM), was utilized in the model simulations. The ACM approach was first proposed by Chorin (1967), and many subsequent experiments and applications have shown it to be an excellent tool to enforce faster convergence in steady state simulations, as well as in highly dynamic simulations (Lee et al., 2006).

Several preliminary numerical runs were conducted to test model sensitivity to the spatial resolution of the calculation domain. Within these simulations, the Δx and Δy resolutions were varied between $D/4 \rightarrow 2D$ (D being the jet discharge diameter), while Δz was varied between $D \rightarrow 4D$ (see Table 2). These simulations were compared directly to experimental data (Malcangio and Mossa, 2016). Figure 2 shows the normalized longitudinal $u\,(x, z)/U_a$ and vertical $w\,(x, z)/U_a$ velocity components plotted for test T2 (see Table 1) as a vertical profile at $x/D = 8$, along with the corresponding concentration $C\,(x, z)$ as defined by:

$$C\,(x, z) = \Delta T\,(x, z)/(\Delta T)_0 = (T\,(x, z) - T_a)/(T_0 - T_a). \quad (7)$$

Here, $T\,(x, z)$ is the mean temperature obtained at each solution node (x, z) in the computational domain. All of them, i.e. $u\,(x, z)/U_a$, $w\,(x, z)/U_a$ and $C\,(x, z)$, are obtained at the centreline ($y/D = 0$). Qualitatively, the best overall agreement between the numerical simulations and the experimental data, plotted in Fig. 2, appears to be obtained with grid 3 (i.e. $\Delta x = \Delta y = D/2$; $\Delta z = D$, Table 2). This is somewhat surprising as discretization errors would be expected to decrease with increasing grid resolution and, hence, grid 4 (i.e. $\Delta x = \Delta y = D/4$; $\Delta z = D$, Table 2) would have been expected to yield the best predictions of the

experimental data. In order to quantify and compare the predictive performance of the model for the different grids tested, statistical indices such as the root-mean-square error (RMSE), the difference in mean values (Δ_{MEAN}) and standard deviation (Δ_{STDEV}) between simulated and measured values, as well as the ratio of RMSE to the standard deviation of the observations (RSR) and the coefficient of determination (R^2), were calculated. These indicators are used generally as model evaluation statistics (e.g. Willmot, 1981; Nash and Sutcliffe, 1970). The RMSE indicates a perfect agreement between observed and predicted values when it equals 0 (zero), with increasing RMSE values indicating an increasingly poor agreement. Similarly, the lower the Δ_{MEAN}, Δ_{STDEV} and RSR values, the better the model simulation performance. Finally, the coefficient of determination, R^2, which ranges between 0 and 1, describes the proportion of the variance in the measured data, which is explained by the model, with higher values, i.e. $R^2 > 0.5$, indicating less error variance. Table 3 presents the results of the statistical analysis for each of the four grids. Although the results cannot be claimed to be grid-independent, the differences between them are considered sufficient to adopt the discretization tested in grid 3 (see Tables 2 and 3) as the most appropriate, especially when compared with the effects of adopting different turbulence models, which will be discussed in the following section.

3.2 Eddy Viscosity and Turbulence Modelling

Together with the optimal choice of the domain grid discretization, there are several ways to define the eddy viscosity for turbulence modelling. An appropriate calibration of the turbulence model must consider the closure problem, which is solved in the turbulence module by the Boussinesq eddy viscosity concept that relates the Reynolds stress tensor to the velocity gradients. The discarded scales of motion act on the resolved velocity field as new stresses, which need to be modelled (Meneveau, 1993). The fact that the modelling is done at a length scale smaller than the flow integral scale raises the hope that the models can be more flow independent than their counterparts for Reynolds stresses. The filtered Navier-Stokes equations are used to find necessary conditions on the statistical properties of the modelled subgrid-scale stress tensor, for statistical equivalence between the measured and the modelled turbulent velocity field, the latter via Large Eddy Simulations (LES). Thus, the effective shear stresses in the momentum equations in MIKE 3 contain the kinematic viscosity, the Reynold stresses (turbulence) and subgrid scale fluctuations. Figure 2 compares the instantaneous vertical profiles of normalized longitudinal $u\,(x, z)/U_a$ and vertical $w\,(x, z)/U_a$ velocities obtained at the end of the model simulations by two of the many different eddy viscosity formulations tested [i.e. the Smagorinsky subgrid scale approach (Fig. 2a) and the constant eddy viscosity approach (Fig. 2b)]. About the second numerical approach, the constant value

of the eddy viscosity (ν_T = 0.005 $m^2 s^{-1}$) was specified over the entire computational domain, meaning that the effect of turbulence was handled equally for all computational cells in the model domain. The qualitative (Fig. 2) and statistical (Table 3) analysis of the comparison between model predictions with the two different turbulence models implemented and tested against experimental data revealed the most appropriate results were obtained with for the pure Smagorinsky formulation. This popular turbulence closure model for the subgrid scale eddy viscosity was, in turn, calibrated by varying the Smagorinsky factor for both the horizontal direction and the vertical direction, independently. The interesting aspect from Fig. 2 is that the numerical results obtained using the Smagorinsky formulation (Fig. 2a), compared to those obtained considering the same grid of calculation, almost follow the experimental data, while those obtained considering a constant eddy viscosity (Fig. 2b) underestimate both the velocity magnitude and the vertical penetration of the jet. Indeed, the results confirm that the current tendency to no longer use models with a constant eddy viscosity formulation, given the level of inaccuracy in their predictions, to be appropriate. In general, it is definitely much better to avoid using a constant eddy viscosity and go for a constant Smagorinsky coefficient. The constant Smagorinsky coefficient means that the eddy viscosity scales with the grid size such that the sub-grid energy increases with length scale.

An additional assessment of computational grid quality can be done by inspecting the one-dimensional power spectra of the velocity components, as suggested by Cavar and Meyer (2012). As known from literature, the inertial subrange, which is the short-wave number subrange of the equilibrium range that is not affected by viscosity, can be described by the Kolmogorov's K−5/3 power law, where K is the wave number (Frisch, 1995). If the computational domain is well discretized, this inertial subrange can be identified by the abovementioned law in the velocity power spectra. Figure 3 shows the power spectra for the velocity components measured at two locations in the computational domain for test T2 (Table 1). These spectra are based on a time series data simulated at a time step frequency f = 2 kHz and consisting of 16,384 samples, using the grid spatial resolution of run 3 ($\Delta x = \Delta y = D/2$; $\Delta z = D$, Table 2). Figure 3 shows that the decay in the one-dimensional power spectra for all velocity components at both domain positions agrees well with the Kolmogorov's K−5/3 power law (i.e. slope of -5/3). This result confirms that effective simulation filtering occurs in the inertial subrange region, which is one of the basic demands for a well resolved numerical calculation (Cavar and Meyer, 2012).

3.3 Model validation

To validate the current numerical methodology in its ability to predict successfully the evolution of a buoyant jet in a cross flow using a large-scale, numerical modelling approach,

the present study compares these model simulations with measured experimental datasets of mean centerline ($y/D = 0$) temperature and velocity fields (Malcangio and Mossa, 2016). Furthermore, an analysis of measured and simulated buoyant jet trajectories is also undertaken to consider additional jet properties on which to improve calibration of the numerical model.

Velocity fields

Velocity measurements in the plane of flow symmetry ($y/D = 0$) are useful for determining the jet penetration within the ambient cross flow, which has been one of the primary objectives of many experimental and theoretical studies of jets discharging into a flowing current (Chochua et al., 2000; Muppidi and Mahesh, 2007; New et al., 2006).

Figure 4 shows vector maps of the flow velocity in the *xz*-plane (i.e. resultant of the streamwise u and vertical w time-averaged velocity components at each computational grid point and measurement location) for test T1 (Fig. 4a) and T2 (Fig. 4b) (see Table 1). It should be pointed out that the use of the ADV system was particularly difficult near the jet nozzle. For this reason, experimental velocity data near the nozzle, i.e.at $x/D < 1$ and at a distance $z/D < 14$ from the channel bottom, have been omitted. In Fig. 4, the evolving flow fields are found to be well described by the measured velocity vectors, with the spreading of the jet and its deflection due to the ambient cross flow clearly shown. Direct comparison of the numerical (blue vectors) and measured (black vectors) velocity fields in Fig. 4 also reveals that the mathematical model closely reproduces these physical phenomena, with a slight overestimation of the velocity vector module. Moreover, the extension of the jet spreading zone seems to be almost identical for both the numerical and experimental velocity fields.

Figure 5 compares the computed and measured vertical (z/D) profiles of the horizontal velocity component u/U_a for the jet evolution in test T2 at six downstream locations $x/D = 2$, 4, 8, 12, 16 and 32 (at $y/D = 0$). The numerically-simulated u/U_a profiles in Fig. 5 are found to be consistent with those measured in laboratory, i.e. both have the same overall structure and evolution with increasing x/D. Moreover, both the simulated and measured velocity profiles show that u/U_a experiences two peaks (i.e. a maximum and minimum) for sections at $x/D \leq 8$. The minimum peak appears in the wake-like region beneath the jet, while the other lies in the jet field and corresponds to the absolute maximum (i.e. the jet velocity axis). The presence of jet zones with mean streamwise velocities that are significantly higher and lower than the ambient mean flow velocity U_a is consistent with experimental results of de Wit et al. (2014) and Sherif and Pletcher (1989). Indeed, the initial near-vertical jet in the MDNF flow region provides an obstruction to the ambient cross flow. Further downstream of the jet source (i.e. for $x/D > 16$), the ambient cross flow dominates,

and the presence of the jet significantly reduces in both the numerical and the experimental velocity vector fields. At this location, it was found that the irregular shapes of the numerical u/U_a profiles is likely to be due to the highly dissipative nature of the Smagorinsky model and depends on tuning of the turbulence model coefficients (see different profiles in Figs. 2a-b).

Figure 6 shows the normalized vertical velocity component profiles w/U_a, again for test T2 (Table 1) at the same x/D positions as shown in Fig. 5. The vertical w/U_a profiles are shown to display good overall quantitative agreement between the computational and experimental data, especially at $x/D = 2$ where the values coincide closely. The maximum w/U_a value diminishes and is observed at a progressively higher z/D elevation as the jet evolves in the downstream x/D direction. This indicates that the impingement of the jet on the cross flow reduces with increasing x/D and its effect is confined to the free surface zone. It is also interesting to note that, in the flow region close to the channel bottom, both experimental and numerical w/U_a values are negative. This result, in accord with the findings in Fig. 5, could be attributed to the shallow nature of the ambient cross flow, which can induce localized or distributed disturbances due to large-scale instabilities in the evolving flow field (Jirka, 2001).

The fundamental characteristic length scales l_m and l_b used in the description of buoyant jet and plume trajectories, respectively, within an ambient cross flow have been studied extensively by List (1982) and Wright (1977) amongst others. In this study, $l_m > l_b$, and the thermal jet can be defined as momentum-dominated, in which the flow regime evolves from a "vertical jet" close to the source [i.e. momentum-dominated near-field (MDNF)] to a "bent jet" with increasing influence from the cross flow [i.e. momentum-dominated far-field (MDFF)] and finally to a "bent plume" [i.e. buoyancy-dominated far-field (BDFF)]. Typically, the transition from a weakly-deflected to strongly-deflected jet trajectory (i.e. from near- to far-field), occurs at a vertical distance $z \sim l_m$. Figure 7 plots the normalized centerline axial jet velocity u_m/U_a versus the non-dimensional vertical distance z/D of the jet axis from the channel bottom. This plot shows good agreement between the experimental and computed data, and with typical slopes found by several authors (Fischer et al., 1979; List, 1982; Rodi, 1982) for momentum-dominated (i.e. $l_m > l_b$) buoyant jets in cross flows. In this case, for the transition between the three abovementioned flow regimes (i.e. MDNF $\rightarrow$ MDFF $\rightarrow$ BDFF), the maximum, time-averaged axial velocity follows a well-known -1 and -1/2 slope sequence, confirming that the simulated free thermal jet is momentum-dominated.

Temperature fields

The mean concentration field is widely used to quantify the penetration behavior for the round buoyant jet discharged into an ambient cross flow. Example color maps of

concentration (i.e. representing the temperature excess $\Delta T/(\Delta T)_0$, Eq. (7)) for numerical and experimental simulation data obtained at $y/D = 0$ are shown in Fig. 8 for tests T2 (Figs. 8a and 8b) and T4 (Figs. 8c and 8d) (see Table 1). In this regard, the simulated results are shown to compare well with the experimental measurements in terms of the evolving jet shape, magnitude, and the horizontal and vertical location of different jet concentration levels, indicating largely an equivalent zone over which the temperature excess reduces from $\Delta T/\Delta T_0 = 0.85 \rightarrow 0.05$, i.e. $x/D = -2 \rightarrow \sim 20$ and $z/D = 12 \rightarrow 36$.

In Fig. 9, the corresponding normalized vertical concentration $[\Delta T\,(z)/(\Delta T)_0]$ profiles for test T2 are plotted at the downstream x/D positions shown in Figs. 5 and 6 at the centerline $y/D = 0$ plane. It is noted that the numerical simulations provide very good agreement with the measured data and, indeed, indicate even better predictive model capabilities for temperature excess fields generated by the thermal jet in the ambient cross flow than the corresponding velocity fields (Figs. 5 and 6).

In order to better understand the additional influence that the ambient current has on jet mixing processes, it is interesting to compare the dilution of the buoyant thermal jet in a cross flow, under consideration in the present study, with empirical laws reported in literature (Noutsopoulos and Yannopoulos, 1987) for a similar jet but released into a stagnant environment. To do this, the experimental and simulated data for the non-dimensional centerline axial jet concentration $C\ [= \Delta T/(\Delta T)_0]$ and its relative vertical elevation z/D, were multiplied by F_0 and F_0^{-1}, respectively, and plotted in Fig. 10 in a similar manner to that reported in Noutsopoulos and Yannopoulos (1987). The resulting experimental and numerical data within the current study are shown to collapse satisfactorily, but also diverge significantly (away from the source) from an analytical expression (Noutsopoulos and Yannopoulos, 1987) derived to determine the dimensionless centerline axial concentration of a round vertical turbulent buoyant jet in quiescent ambient fluid. With increasing distance (z/D) from the source, the dilution of the momentum-dominated thermal jet in the cross flowing ambient deviates from that of a similar buoyant jet discharging into a stagnant ambient. The main difference is that the concentrations (i.e. temperature excess) decreases more rapidly due to additional mixing and entrainment effects from the ambient current, resulting in enhanced dilution characteristics, as indicated in Fig. 10.

The results discussed so far have confirmed that the thermal jets analyzed are momentum dominated and can be properly scaled by the length scale l_m. This latter aspect will be verified in the next section. In this context, Fig. 11 shows the distribution of the centerline dilution normalized by l_m with all experimental and numerical data shown to collapse on the same trend, typical of momentum driven buoyant flows. Moreover, Fig. 11 also demonstrates a very clear transition from the MDNF to MDFF flow regimes when the

normalised jet elevation z/l_m approaches unity. This trend, and the change of slope for near- and far-field dilution characteristics, are again valid for both experimental data and numerical simulations. A number of empirical relationships for dilution for buoyant jets in cross flows are available from previous studies, within which the empirical model coefficients have been determined by means of fitting to both laboratory and field experimental data. In this regard, Fig. 11 shows excellent agreement in the comparison of current data with a previous empirical near- and far-field dilution model (Wright, 1984) (i.e. solid lines) for vertical momentum dominated jets discharging into an unstratified ambient cross flow, with the same empirical model coefficients. Therefore, the appropriateness of the far-field circulation model response in reproducing the near-field and far-field dilution processes for a turbulent thermal buoyant jet in a cross flow, can be considered as highly satisfactory.

Jet trajectories

The jet trajectory in a cross flow is one of the most widely investigated features in previous studies (Pratte and Baines, 1967; Rajaratnam, 1976; Andreopoulos and Rodi, 1984), largely because it represents the spatial evolution of the jet within the ambient flow field, revealing both the rising height and inflection trends in the evolving jet. Within the current study, the experimental and computational jet trajectories are obtained by tracing the maximum temperature (Fig. 12a) and velocity (Fig. 12b) in corresponding simulated and measured *xz*-fields obtained on the plane of flow symmetry ($y/D = 0$), for a longitudinal extent ranging from $x/D = 0$ to $x/D = 20$ (beyond which measured data was not available). The normalised vertical distance z'/D in Fig. 12 is defined from the jet source exit elevation (i.e. $z' = z - h_0$) above the channel bottom. The locations of the maximum temperature and velocity were outlined within the flow domain by multiple point measurements, instead of analysing the maximum visual rise of the buoyant jet by image processing as done in previous studies (Cavar and Meyer, 2012; Meyer et al., 2007). Figure 12 shows both calculated and measured trajectories for all test cases, except for the first experiment (test T1, Table 1), where only the velocity measurement data were available (Fig. 12b). All trajectories shown in Fig. 12 indicate similar jet trajectory development, following reasonably well the empirical correlations proposed in previous studies on circular jets in cross flows (see Table 4) (Rajaratnam, 1976). More detailed analysis of Fig. 12 shows that at a vertical distance $z'/D < 10$, the effects of the cross flow in deflecting the jet appear to be negligible. Further downstream in the far-field region, where mixing and entrainment processes are governed by ambient currents, the maximum values of temperature and velocity gradually diminish, and jet trajectories are deflected by the ambient cross flow. Considering first the temperature data (Fig. 12a), the simulated trajectories lie slightly lower than the experimental measurements,

possibly due to slightly higher mixing and dilution in the numerical simulations. However, for test T2, where more experimental data are available in the far-field flow region $x/D > 12$ compared to other tests, the numerical and experimental trajectories are shown to largely coincide in this region. When comparing the jet trajectories based on the maximum velocity data (Fig. 12b), the modelled trajectories are shown to coincide well with measured ones throughout the far-field region and, to a certain extent, within the near-field region.

In Fig. 13, the measured and calculated trajectories are represented in a double-logarithmic plot and scaled by the length scales l_m (Fig. 13a) and l_b (Fig. 13b). Figure 13a shows that the trend of the computed trajectories follows the empirical relations reported in literature (Wright, 1984) satisfactorily for momentum-dominated buoyant jet in a cross flow. Moreover, the slopes of the jet trajectories indicate different exponents for power laws in the weakly (MDNF) and strongly (far-field) deflected stages, intersecting at $z' \approx l_m$. In Fig. 13b, the computed trajectories deviate more significantly from the typical slopes of 3/4 and 2/3 for the buoyancy-dominated near-field (BDNF) and far-field (BDFF) flow regimes, respectively. It therefore follows that scaling based upon the buoyancy-to-cross flow length scale l_b is not appropriate to the type of thermal jet discharge under consideration here, which can be regarded as weakly-buoyant. As such, the greater importance of the initial momentum flux M in the flow development is confirmed through normalizing the trajectory ordinates (x, z) by the momentum-to-cross flow length scale l_m in Fig. 13a. More importantly, the results from the simulated trajectories suggests that the large-scale, far field model used for this study successfully simulate a heated buoyant jet discharged from a submerged round port in a flowing ambient environment, in all its development.

4 Conclusions

RANS simulations and experimental measurements of circular, turbulent thermal jets in ambient cross flows are presented in this paper. The numerical results, generated using the MIKE 3 simulation tool, are found to be in good agreement with the measured experimental data, indicating that the model, mainly utilized for large-scale, far-field hydrodynamic studies, is also capable of correctly capturing the near-field flow and mixing of thermal jets discharging into flowing ambient fluids. The validity of the numerical results, which is tested in direct comparisons with laboratory data, is found to be strongly dependent on (i) the spatial resolution of the numerical grid, and (ii) selection of an appropriate turbulence model. Some difficulties are experienced when using the classical RANS model to reproduce the velocity vector fields generated in the experimental study, especially with an over-prediction of maximum values for the vertical velocity components. However, in terms of predicting the scalar (excess temperature) field, the RANS model simulations show good overall agreement

with the experimental data.

The experimental and numerical results also indicate that the source momentum flux has a strong influence on the basic characteristics and behavior of the thermal buoyant jets in ambient cross flows, with buoyancy flux playing a relatively minor role in jet dynamics. Therefore, only the specific momentum-to-ambient flow length scale l_m needs to be considered for the analysis of the jet trajectories, dilution and spreading. Similarly, the influence of the ambient current, even if with a relatively small cross-flow velocity, is shown to have a significant beneficial effect on the jet mixing and dilution processes, compared to vertical buoyant jet discharges into stagnant ambient fluid bodies. Finally, measured and simulated buoyant jet trajectories were also derived from both the maximum temperature and velocity data and shown to follow the same trends for both the numerical and experimental configurations. These trajectory data are also in good agreement with the findings from several previous studies.

Overall, the novelty of this study arises from the successful application of a widely-used, "industry-standard" flow simulation tool, utilized more generally for far-field studies of free surface flows, sediment dynamics and water quality processes, in the prediction of near-field flow dynamics and mixing associated with thermal buoyant jet discharges in the marine environment. The applicability of this modelling tool to simulate the smaller-scale dynamics of these near-source processes clearly opens up new possibilities to consider the whole "source-to-sink" flow field for marine wastewater discharges within a single modelling tool, i.e. through nesting of structured near-field and far-field model domains. As such, this also presents the potential to improve current modelling techniques utilised by engineers and environmental regulators for the assessment of water quality compliance from existing marine wastewater discharges and during the design phase, in terms of ensuring initial dilution requirements are met. Such a nested, multi-scale modelling approach could also be potentially extended to investigate other types of marine wastewater discharges, such as particle-laden buoyant jets or hypersaline discharges from desalination plants.

Acnowledgements

The authors would like to thank Andrea Pedroncini, DHI Italy, for the technical advice provided by during the numerical modeling phase of the study. The insightful comments of two anonymous reviewers and the Associate Editor are also acknowledged as leading to significant improvements to the overall paper.

References

Abraham, G. (1963). Jet Diffusion in Stagnant Ambient Fluid. Delft Hydraulics Lab., Publ. No. 29.

Abramovich, G. (1963). *The Theory of Turbulent Jets*. Cambridge: MIT Press.

Andreopoulos, J., & Rodi, W. (1984). Experimental investigation of jets in a crossflow. *Journal of Fluid Mechanics, 138*, 93-127.

Arunajatesan, S. (2012). *Evaluation of two-equation RANS models for simulation of jet-in-crossflow problems*. Paper presented at the Fiftieth AIAA Aerospace Sciences Meeting, Nashville, US.

Ben Meftah, M., De Serio, F., Malcangio, D., & Mossa, M. (2014, September). Vegetation effects on vertical jet structures. In A. J. Schleiss, G. de Cesare, M. J. Franca, & M. Pfister (Eds.), *CRC Press. Proceedings of River Flow 2014* (pp. 581-588), Lausanne, CH: EPFL.

Ben Meftah, M., De Serio, F., Malcangio, D., Mossa, M., & Petrillo, A.F. (2015). Experimental Study of a Vertical Jet in a Vegetated Crossflow. *Journal of Environmental Management, 164,* 19-31.

Ben Meftah, M., Malcangio, D., De Serio, F., & Mossa, M. (2018). Vertical dense jet in flowing current. *Environmental Fluid Mechanics, 18(1)*, 75-96.

Blumberger, A. F., Ji, Z.-G., & Ziegler, C. K. (1996). Modelling outfall plume behavior using far field circulation model. *Journal of Hydraulic Engineering, 122(11)*, 610-616.

Cavar, D., & Meyer, K. E. (2012). LES of turbulent jet in cross-flow: Part 1 – A numerical validation study. *International Journal of Heat and Fluid Flow, 36*, 18-34.

Chochua, G., Shyy, W., Thakur, S., Brankovic, A., Lienau, J., Porter, L., & Lischinsky, D. A (2000). Computational and Experimental Investigation of Turbulent Jet and Crossflow Interaction. *Numerical Heat Transfer, Part A: Applications, 38*, 557-572.

Chorin, A. J. A (1967). Numerical Method for Solving Incompressible Viscous Flow Problems. *Journal of Computational Physics, 2*, 12-26.

Chu, V. H., & Goldberg, M. B. (1974). Buoyant forced-plumes in cross flow. *Journal of Hydraulic Division, 100(HY9)*, 1203-1214.

Cuthbertson, A. J. S., & Davies, P. A. (2008). Deposition from particle-laden, round, turbulent, horizontal, buoyant jets in stationarfy and coflowing receiving fluids. *Journal of Hydraulic Engineering, 134(4)*, 390-402.

de Wit, L., van Rhee, C., & Keetels, G. (2014). Turbulent Interaction of a Buoyant Jet with Cross-Flow. *Journal of Hydraulic Engineering, 140(12),* 1-14.

DHI Software (2009). MIKE 3. Estuarine and Coastal Hydraulics and Oceanography. User Guide, Horsholm, Denmark.

Doneker, R. L., & Jirka, G. H. (2007). CORMIX User Manual: A Hydrodynamic Mixing Zone Model and Decision Support System for Pollutant Discharges into Surface Waters. EPA-823-K-07-001.

Fan, L. N. (1967). Turbulent Buoyant Jets into Stratified or Flowing Ambient Fluids. Report No. KH-R-15, W.M. Keck Laboratory of Hydrology and Water Resources, California Institute of Technology, Pasadena, CA.

Fischer, H. B., List, E. J., Koh, R. C. Y., Imberger, J., & Brooks, N. H. (1979). *Mixing in Inland and Coastal Waters.* New York: Academic Press.

Frisch, U. (1995). *Turbulence: the legacy of A.N. Kolmogorov*. Cambridge: Cambridge University Press.

Gao, M., Huai, W., Xiao, Y., Yang, Z., & Ji, B. (2018). Large eddy simulation of a vertical buoyant jet in a vegetated channel. *International Journal of Heat and Fluid Flow, 70,* 114–124.

Gohil, T. B., Saha, A. K., & Muralidhar, K. (2011). Direct Numerical Simulation of Naturally Evolving Free Circular Jet. *Journal of Fluids Engineering, 133(11),* 111203.

Guan, H., & Wu, C. (2007). Large-eddy simulations and vortex structures of turbulent jets in crossflow. *Science in China Series G: Physics, Mechanics & Astronomy, 50(1),* 118–132.

Holdeman, J. D., & Srinivasan, R. (1984). On Modelling Dilution Jet Flow Fields. *NASA TM-83708*, Cleveland, OH.

Hwang, R.-R., Chiang, T.-P., & Yang, W.-C. (1995). Effect of ambient stratification on buoyant jets in crossflow. *Journal of Engineering Mechanics, 121*, 865-872.

Jirka, G. H. (2001). Large scale flow structures and mixing processes in shallow flows. *Journal of Hydraulic Engineering, 39(6),* 567-573.

Jirka, G. H. (2004). Integral Model for Turbulent Buoyant Jets in Unbounded Stratified Flows. Part I: Single Round Jet. *Environmental Fluid Mechanics, 4(1),* 1-56.

Jirka, G. H. (2006). Integral Model for Turbulent Buoyant Jets in Unbounded Stratified Flows Part 2: Plane Jet Dynamics Resulting from Multiport Diffuser Jets. *Environmental Fluid Mechanics, 6(1),* 43-100.

Jones, W. P., & McGuirk, J. J. (1980). *Computation of a Round Turbulent Jet Discharging into a Confined Crossflow*. In L. Bradbury (Ed.), *Springer Verlag. Proceedings of Turbulent Shear Flow II* (pp. 233-245), Berlin, DE.

Kamotani, Y., & Greber, I. (1972). Experiments on a Turbulent Jet in a Cross Flow. *AIAA J., 10*, 1425-1429.

Lee, J. H. W., & Neville-Jones, P. (1987). Initial dilution of horizontal jet in crossflow. *Journal of Hydraulic Engineering, 113(5)*, 1651-1675.

Lee, J. H-W, & Vincent, C. (2003). *Turbulent Jets and Plumes. A Lagrangian Approach*. Boston: Springer.

Lee, J. W., Teubner, M. D., Nixon, J. B., & Gill, P. M. (2006). Applications of the artificial compressibility method for turbulent open channel flows. *International Journal of Numerical Methods in Fluids, 51*, 617–633.

Lessin, G., & Raudsepp, U. (2006). Water quality assessment using integrated modelling and monitoring in Narva Bay, Gulf of Finland. *Environmental Modeling & Assessment, 11(4)*, 315–332.

List, E. J. (1982). Turbulent jets and plumes. *Annual Review of Fluid Mechanics, 14*, 189-212.

Lumborg, U. (2005). Modelling the deposition, erosion, and flux of cohesive sediment through Oresund. *Journal of Marine System, 56(1)*, 179–193.

Ma, F., Satish, M., & Islam, M. R. (2007). Large eddy simulation of thermal jets in cross flow. *Engineering Applications of Computational Fluid Mechanics, 1(1)*, 25-35.

Malcangio, D., & Mossa, M. (2016). A laboratory investigation into the influence of a rigid vegetation on the evolution of a round turbulent jet discharged within a cross flow. *Journal of Environmental Management, 173*, 105-120.

Malcangio, D., & Petrillo, A.F. (2010). Modelling of Brine Outfall at the Planning Stage of Desalination Plants. *Desalination, 254*, 114-125.

Malcangio, D., Ben Meftah, M., & Mossa, M. (2016). *Physical modelling of buoyant effluents discharged into a cross flow*. Paper presented at the IEEE Workshop on Environmental, Energy, and Structural Monitoring Systems, Bari, IT.

Malcangio, D., Melena, A., Damiani, L., Mali, M., & Saponieri, A. (2017). Numerical study of water quality improvement in a port through a forced mixing system. *WIT Transactions on Ecology and the Environment, 220*, 69-80.

Malcangio, D., Mossa, M., Petrillo, A.F., & Semeraro, A. M. (2008). Experimental Study of the Impact of Rigid Vegetation on a Buoyant Jet in Presence of Crossflows. In M. Altinakar, M. Kokpinar, Y. Darama, B. Yegen, & N. Harmancioglu (Eds.), *KUBABA Congress Department and Travel Service. Proceedings of River Flow 2008* (pp. 875-882), Çeşme – İzmir, TR: KUBABA Congress Department and Travel Service.

Mali, M., Malcangio, D., Dell'Anna, M. M., Damiani, L., & Mastrorilli, P. (2018). Influence of hydrodynamic features in the transport and fate of hazard contaminants within touristic ports. Case study: Torre a Mare (Italy). *Heliyon, 4(1),* e00494.

Meneveau, C. (1993). Statistics of turbulence subgrid-scale stresses: Necessary conditions and experimental tests. *Physics of Fluids, 6(2*), 815-833.

Meyer, K., Pedersen, J., & Özcan, O. (2007). A turbulent jet in crossflow analysed with proper orthogonal decomposition. *Journal of Fluid Mechanics, 583,* 199-227.

Moore, D. J. (1966). Physical aspects of plume models. *Air &Water Pollution, 10,* 411-417.

Muppidi, S., & Mahesh, K. (2007). Direct Numerical Simulation of Round Turbulent Jets in Crossflow. *Journal of Fluid Mechanics, 574,* 59-84.

Nash, J.E., & Sutcliffe, J.V. (1970). River flow forecasting through conceptual models: Part 1. A discussion of principles. *Journal of Hydrology, 10,* 282–290.

New, T. H., Lim, T.T., & Luo, S. C. (2006). Effects of Jet Velocity Profiles on a Round Jet in Cross-flow. *Experiments in Fluids, 40,* 859-875.

Noutsopoulos, G., & Yannopoulos, P. (1987). The round vertical turbulent buoyant jet. *Journal of Hydraulic Research, 25(4),* 481-502.

Patrick, M. A. (1967). Experimental investigation of the mixing and penetration of a round turbulent jet injected perpendicularly into a transverse stream. *Trans. Institute of Chemical Engineers, 45,* 16-31.

Pietrzak, J., Jakobson, J. B., Burchard, H., Jacob Vested, H., & Petersen, O. (2002). A three-dimensional hydrostatic model for coastal and ocean modelling using a generalised topography following co-ordinate system. *Ocean Modelling, 4,* 173–205.

Pratte, B. D., & Baines, W. D. (1967). Profiles of the round turbulent jet in a cross flow. *Journal of Hydraulic Division, 93(HY6),* 53-64.

Priestly, C. H. B. (1956). A working theory of the bent-over plume of hot gas. *Quarterly Journal of the Royal Meteorological Society, 82,* 165-176.

Rajaratnam, N. (1976). *Turbulent Jets*. Amsterdam: Elsevier Scientific Publishing Company.

Roberts, P. J. W., Salas, H. J.; Reiff, F. M., Libhaber, M., Labbe, A., & Thomson, J. C. (2010). *Marine Wastewater Outfalls and Treatment Systems*. London: IWA Publishing.

Rodi, W. (1982). *Turbulent Buoyant Jets and Plumes*, Oxford: Pergamon Press Ltd.

Shahryar, G., & Moshfegh, B. (2013). Evaluation of RANS Models in Predicting Low Reynolds, Free, Turbulent Round Jet. *Journal of Fluids Engineering, 136(1),* 011201.

Sherif, S. A., & Pletcher, R. H. (1989). Measurements of the flow and turbulence characteristics of round jets in crossflow. *Journal of Fluids Engineering, 111*, 165-171.

Sotiropulos, F. (2005). Introduction to statistical turbulence modelling for hydraulic engineering flows. In P. D. Bates, S. N. Line & R. I. Ferguson (Eds.), *Computational Fluid Dynamics: Applications in Environmental Hydraulics*, Chichester: John Wiley & Sons Ltd.

Tang, H. S., Paik, J., Sotiropoulos, F., & Khangaonkar, T. (2008). Three-dimensional numerical modelling of initial mixing of thermal discharges at real-life configurations. *Journal of Hydraulic Engineering, 134(9),* 1210-1224.

Vested, H. J., Justesen, P., & Ekebjaerg, L. (1992). Advection-dispersion modelling in three dimensions. *Applied Mathematical Modelling, 16*, 506-519.

Willmott, C. J. (1981). On the validation of models. *Physical geography, 2(2),* 184-194.

Wright, S. J. (1977). Mean Behavior of Buoyant Jets in a Crossflow. *Journal of Hydraulic Division, 103(HY5),* 499-513.

Wright, S.J. (1984). Buoyant jets in density-stratified crossflow. *Journal of Hydraulic Engineering, 110,* 643-656.

Yang, Li, Ligrani, P., Ren, J., & Jiang, H. (2015). Unsteady Structure and Development of a Row of Impingement Jets, Including Kelvin–Helmholtz Vortex Development. *Journal of Fluids Engineering,* 137(5), 051201.

Zeng, Y.-H., & Huai, W.-X. (2008). Characteristics of round thermal discharging in a flowing environment. *Journal of Hydro-environment Research, 2*, 164-171.

Zhang, X. Y., & Adams, E. E. (1999). Prediction of near field plume characteristics using a far field circulation model. *Journal of Hydraulic Engineering, 125(3),* 233-241.

List of tables

List of figures

Figure 11. Centerline normalized dilution distribution. Comparison of data with integral model prediction by Wright (1984)

Figure 12 Centreline thermal jet trajectories obtained from analysis of (a) maximum temperatures T_m, and (b) maximum velocities U_m in experimental (exp) and numerical (calc) model results

Figure 13 Scalar jet trajectories obtained by experiments and computations, with different scaling (a) l_m, (b) l_b. Comparison of data with integral model prediction by Wright (1984)

Table 1 Main characteristics of the experimental and numerical tests

Test	ΔT_0 (°C)	U_0 (m s^{-1})	g'_0 (m s^{-2})	F_0	r	r_{eff}	Re_0 ($\times 10^4$)	l_M (cm)	l_m (cm)	l_b (cm)
T1	25	1.28	0.09	59.71	15.01	14.94	4.59	28.10	6.65	0.37
T2	35	1.44	0.14	55.15	16.92	16.80	5.87	25.95	7.50	0.63
T3	35	1.92	0.14	72.73	22.72	22.56	7.85	34.23	10.07	0.87
T4	25	1.95	0.09	92.11	22.94	22.83	7.00	43.35	10.16	0.56

Table 2 Summary of the horizontal ($\Delta x = \Delta y$) and vertical (Δz) resolution of the computation grids

Grid	Δx, Δy	Δz
1	$2D$	$4D$
2	D	D
3	$D/2$	D
4	$D/4$	D

Table 3 Values of statistical indices used to evaluate the model performance

		Smagorinsky model (Fig. 2a)				Constant eddy viscosity model (Fig. 2b)			
		Grid 1	Grid 2	Grid 3	Grid 4	Grid 1	Grid 2	Grid 3	Grid 4
u/U_a	RMSE	0.579	0.328	0.150	0.298	0.275	0.291	0.310	0.287
	Δ_{MEAN}	0.380	0.297	0.132	0.075	0.100	0.111	0.104	0.085
	Δ_{STDEV}	0.181	0.041	0.004	0.156	0.259	0.183	0.162	0.184
	RSR	2.134	1.332	0.610	1.210	1.011	1.181	1.258	1.164
	R^2	0.059	0.617	0.826	0.147	0.011	0.001	0.000	0.001
w/U_a	RMSE	1.280	0.354	0.404	0.421	0.626	0.522	0.541	0.525
	Δ_{MEAN}	1.058	0.280	0.253	0.322	0.446	0.123	0.049	0.182
	Δ_{STDEV}	0.305	0.132	0.151	0.061	0.429	0.170	0.113	0.206
	RSR	2.758	0.829	0.946	0.987	1.348	1.224	1.269	1.230
	R^2	0.088	0.862	0.678	0.661	0.012	0.031	0.025	0.043
C	RMSE	0.039	0.037	0.023	0.021	0.075	0.037	0.051	0.096
	Δ_{MEAN}	0.010	0.007	0.013	0.016	0.026	0.002	0.000	0.013
	Δ_{STDEV}	0.000	0.019	0.007	0.006	0.025	0.002	0.025	0.079
	RSR	1.253	1.197	0.745	0.665	2.414	1.175	1.644	3.067
	R^2	0.021	0.384	0.706	0.799	0.227	0.061	0.088	0.143

Table 4 Previous empirical correlations describing the centreline trajectory of circular jet discharges in a cross flowing ambient, with $r = U_0 / U_a$

Authors	Equations
Ivanov (1952), see [56]	$z/D = r^{0.87}(x/D)^{0.33}$
Shandorov (1957), see [56]	$z/D = r^{0.79}(x/D)^{0.39}$
Patrick (1967) [57]	$z/D = r^{0.85}(x/D)^{n}$ (n = 0.38 for velocity measurements) (n = 0.34 for concentration measurements)
Pratte and Baines (1967) [33]	$z/(rD) = 2.05[\ x/(rD)]^{0.28}$

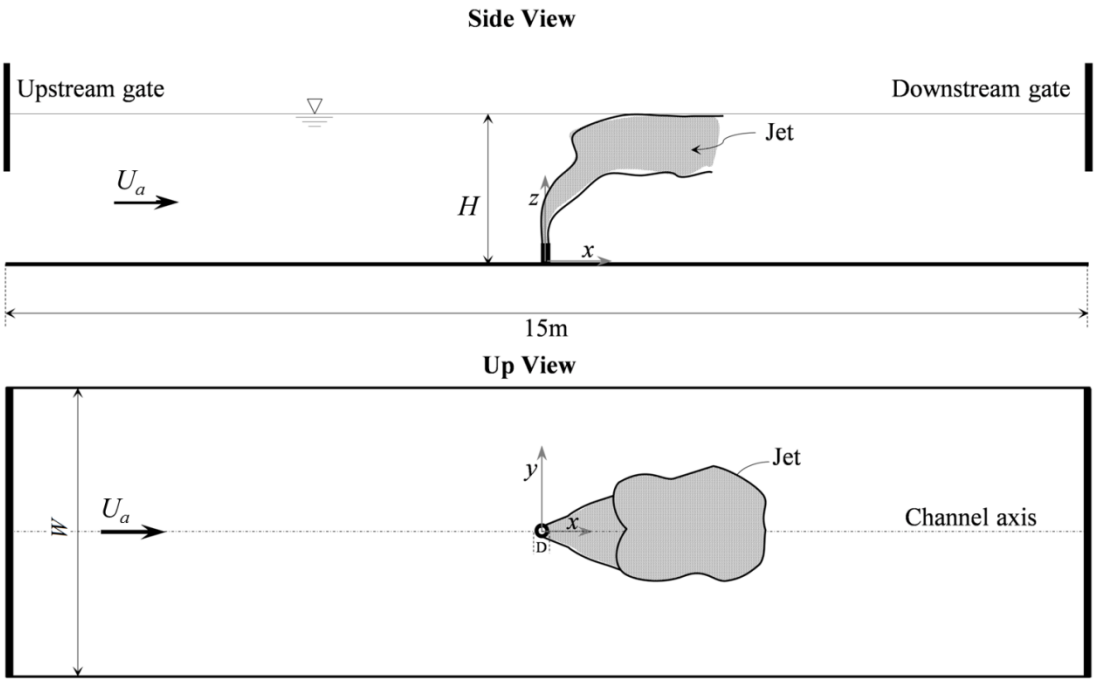

Figure 1 Schematic definition of problem, with horizontal and lateral setting of the axial coordinate system

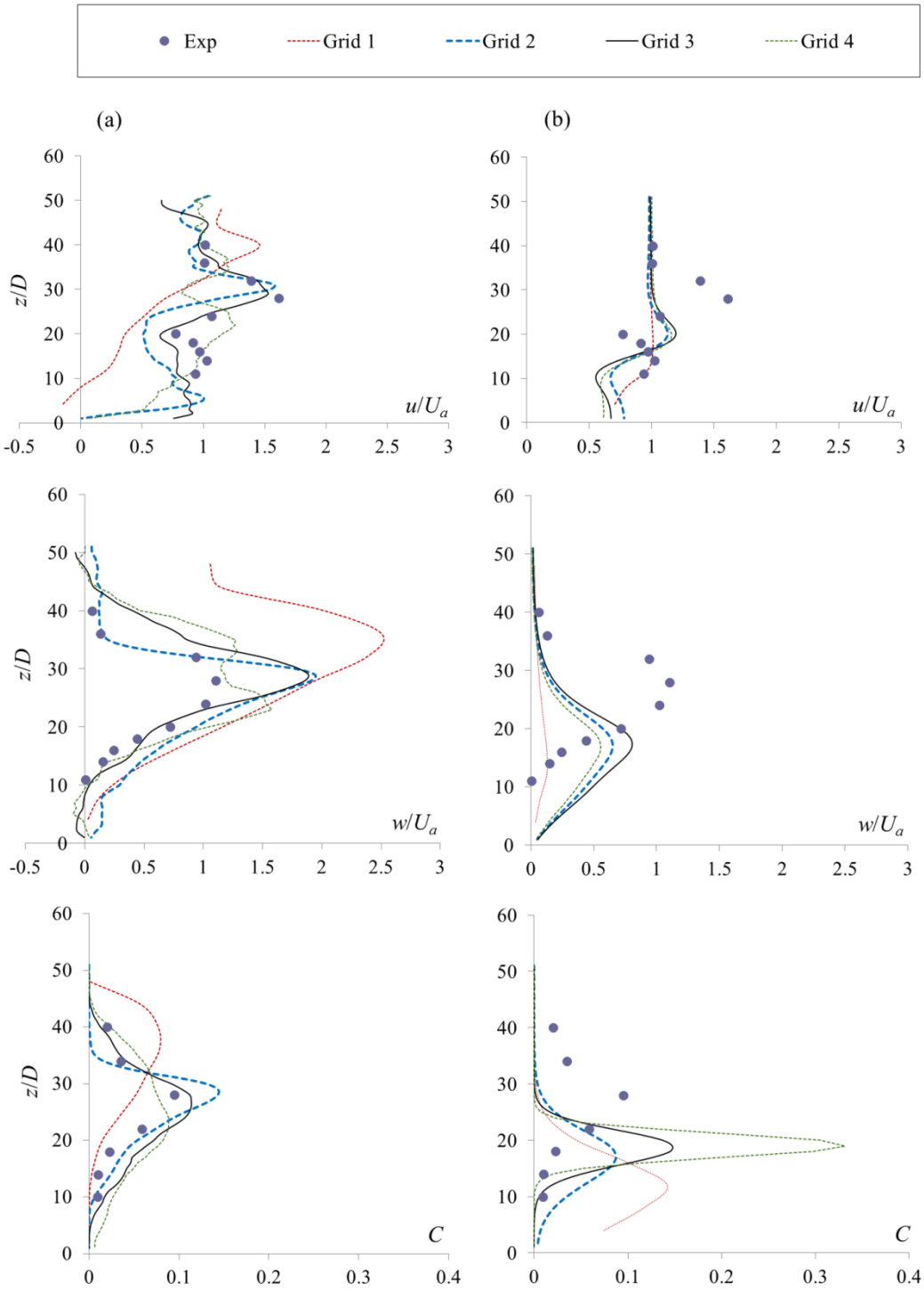

Figure 2 Vertical profiles of normalized horizontal and vertical velocity components (u/U_a and w/U_a) and of concentration C in $y/D = 0$ plane at $x/D = 8$ (for test T2, Table 1). Experimental data (Malcangio and Mossa, 2016) shown as filled circles, numerical simulations shown as lines (see Table 2), with eddy viscosity defined by (a) the Smagorinsky subgrid scale model, and (b) the constant eddy viscosity model ($\nu_T = 0.005$ m^2 s^{-1})

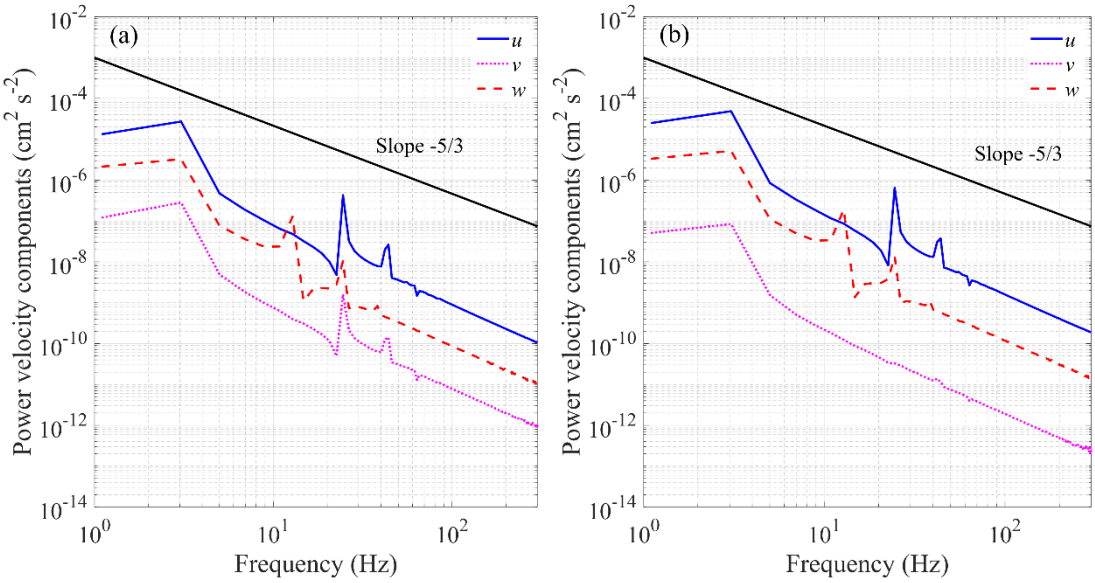

Figure 3 Power spectrum densities of all three velocity components (u, v, w) based on time series data obtained in test T2 (Table 1) at domain positions (a) $x = 2D$, $z = 3D$, (b) $x = 6D$, $z = 4D$ (for $y/D = 0$ in both cases)

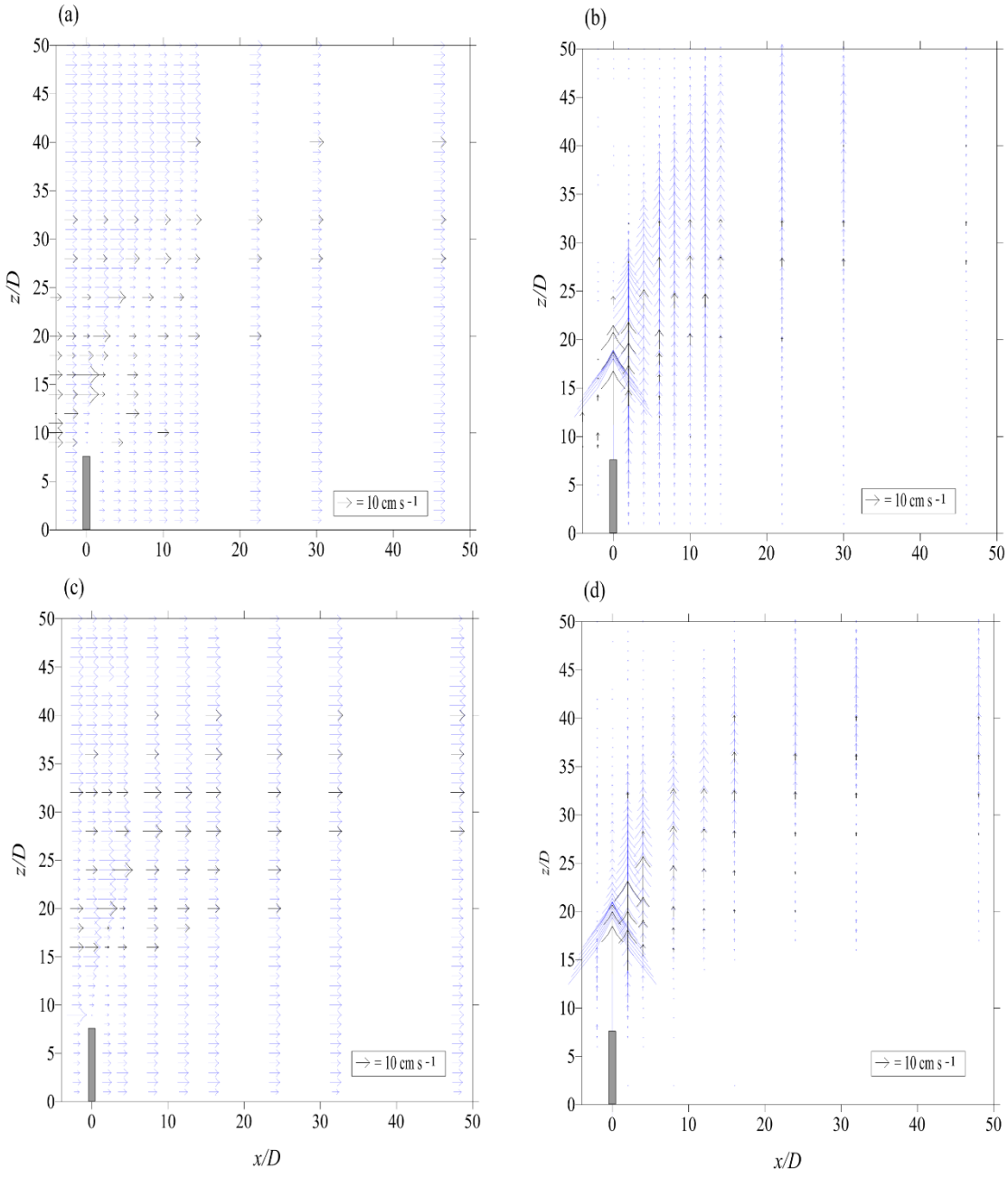

Figure 4 Numerical (blue vectors) and experimental (black vectors) normalized (a) (c) horizontal, (b) (d) vertical, velocity components along the centreline $y/D = 0$ plane for test (a) (b) T1, (c) (d) T2 (see Table 1)

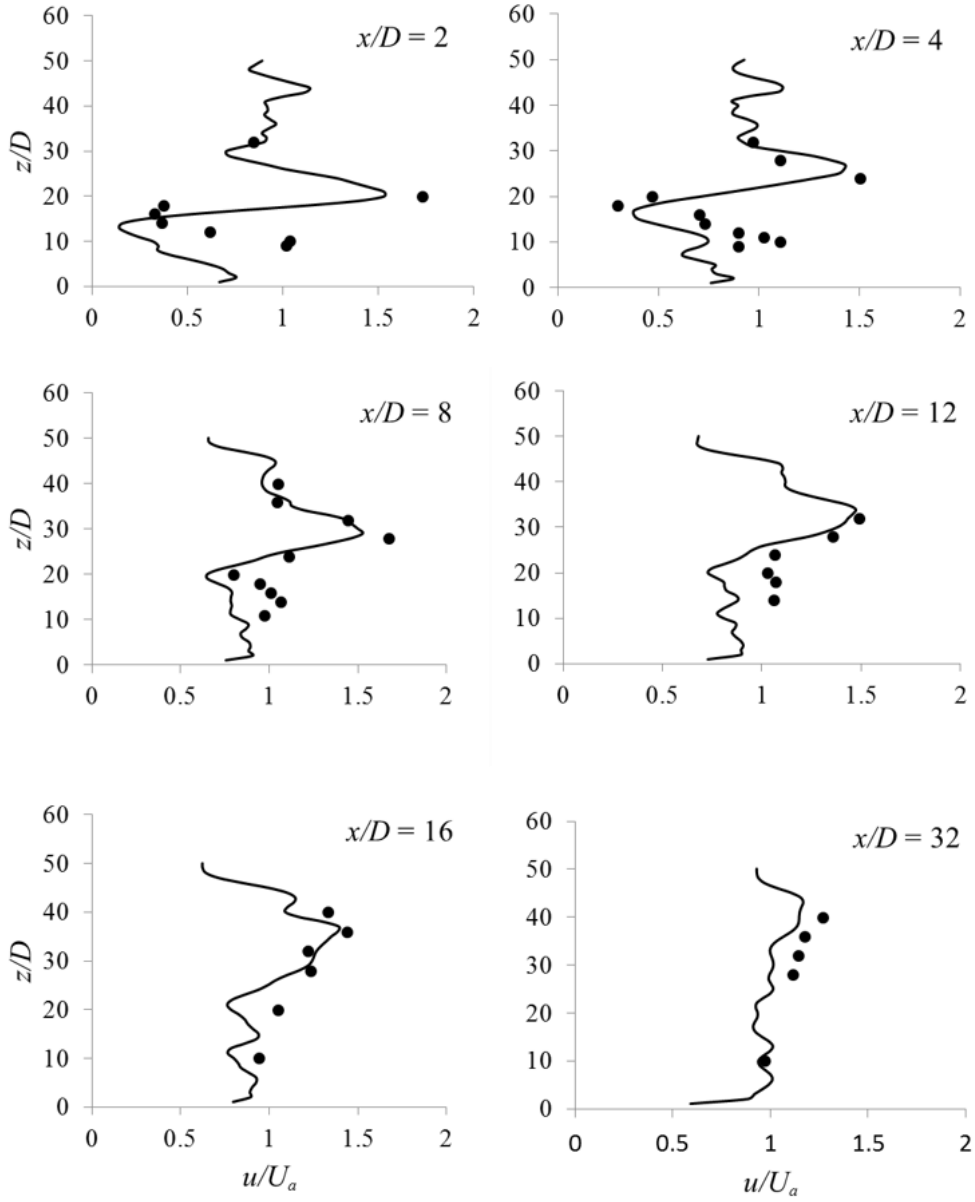

Figure 5 Vertical profiles of normalized horizontal velocity component u/U_a in y/D=0 plane (solid line: calculation; symbols: experiments) at different x/D positions for test T2 (Table 1)

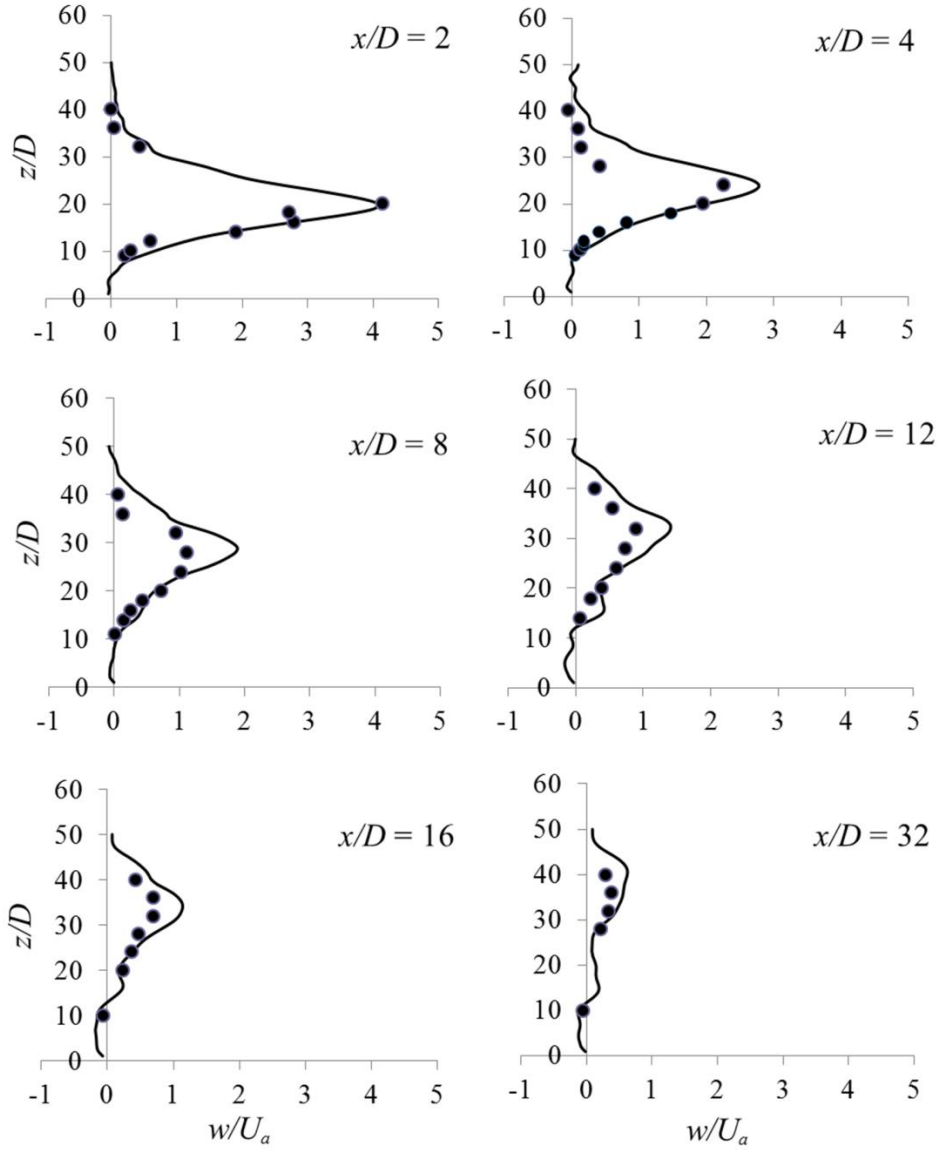

Figure 6 Vertical (*z/D*) profiles of normalized vertical velocity component w/U_a at the $y/D = 0$ plane for test T2 (solid line: calculation; symbols: experiments), measured at different *x/D* positions

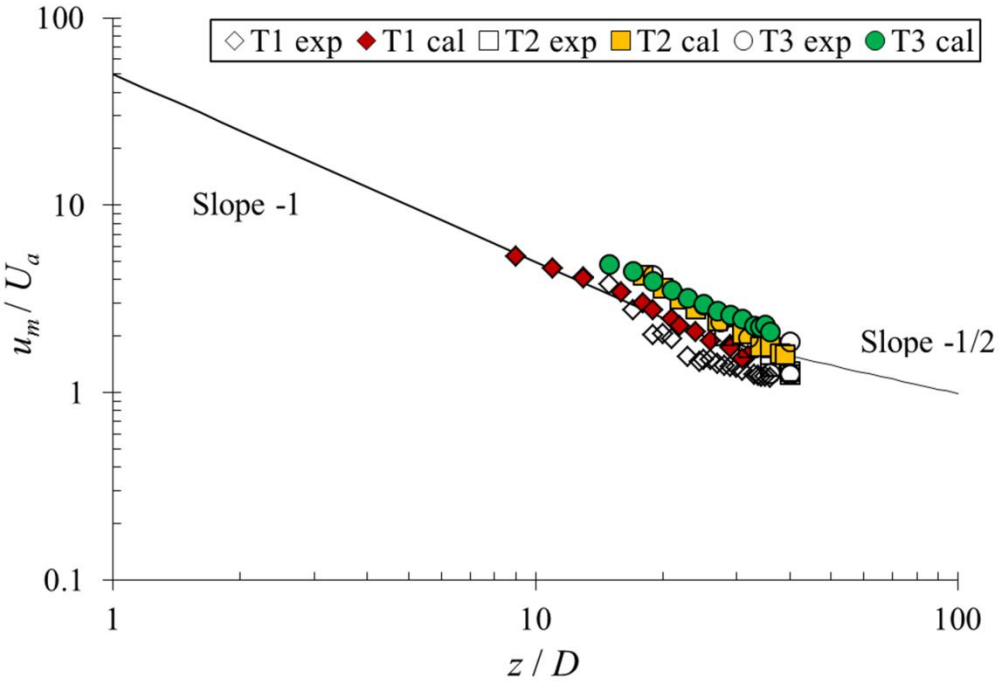

Figure 7 Velocity ratio of centerline axial velocity to ambient cross flow u_m/U_a versus the non-dimensional vertical elevation z/D of the jet axis above the channel bottom

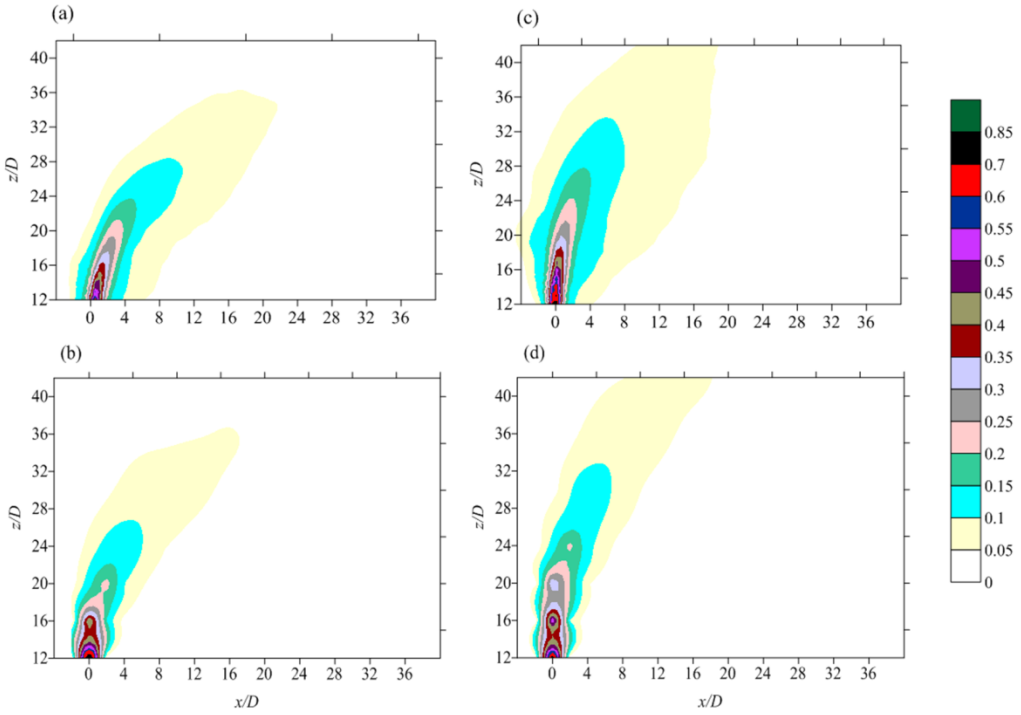

Figure 8 Normalized temperature excess [$C\ (x, z) = \Delta T\ (x, z)/(\Delta T)_0$] fields obtained at the $y/D = 0$ plane from the thermal buoyant jet discharge into an ambient cross flow showing test (a) T2 (simulated), (b) T2 (measured), (c) T4 (simulated), and (d) T4 (measured).

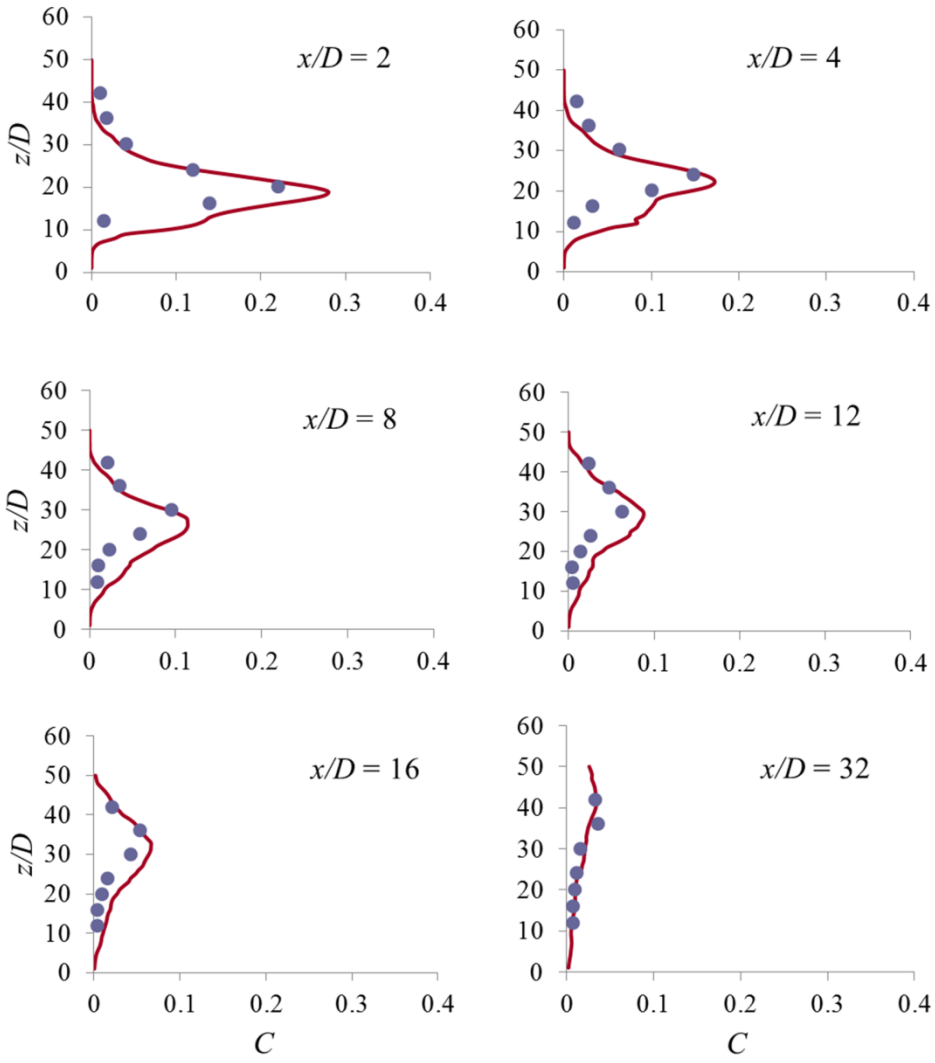

Figure 9 Non-dimensional vertical profiles of normalized temperature excess [C (z) = $\Delta T(z)/(\Delta T)_0$] for test T2 in the y/D = 0 plane (solid lines: numerical predictions; symbols: experimental measurements)

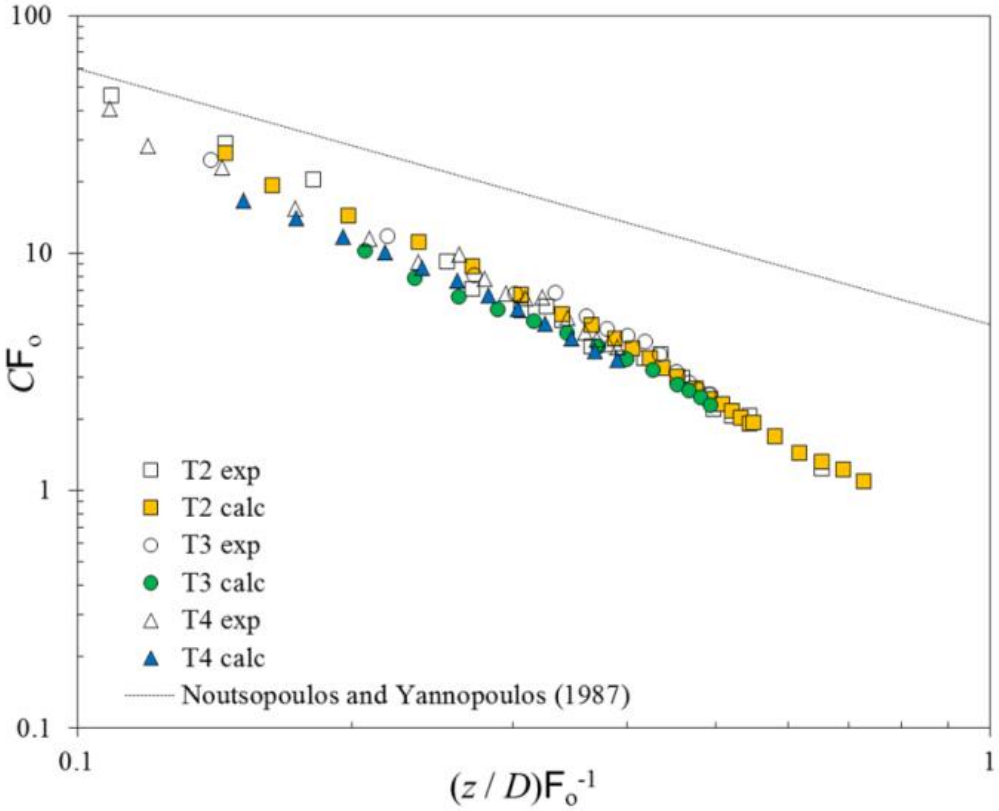

Figure 10 Centerline normalized axial concentrations for thermal jet discharges into an ambient cross flow. Dotted line shows equivalent analytical relationship for vertical buoyant jet discharge into a stagnant ambient (Noutsopoulos and Yannopoulos, 1987)

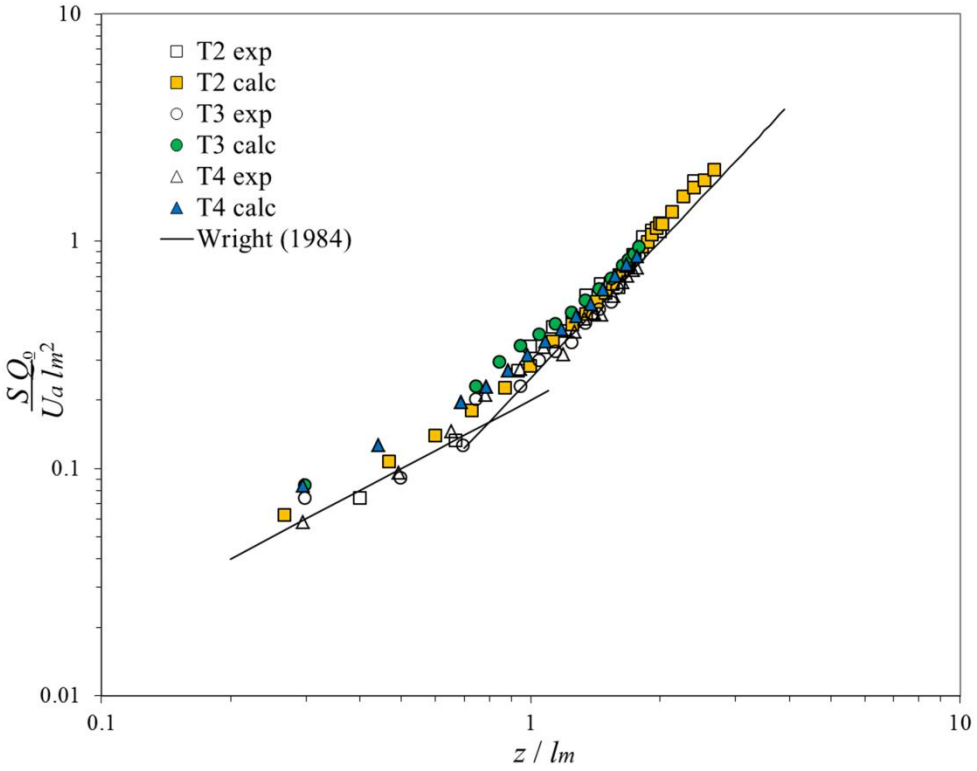

Figure 11 Centerline normalized dilution distribution. Comparison of data with integral model prediction by Wright (1984)

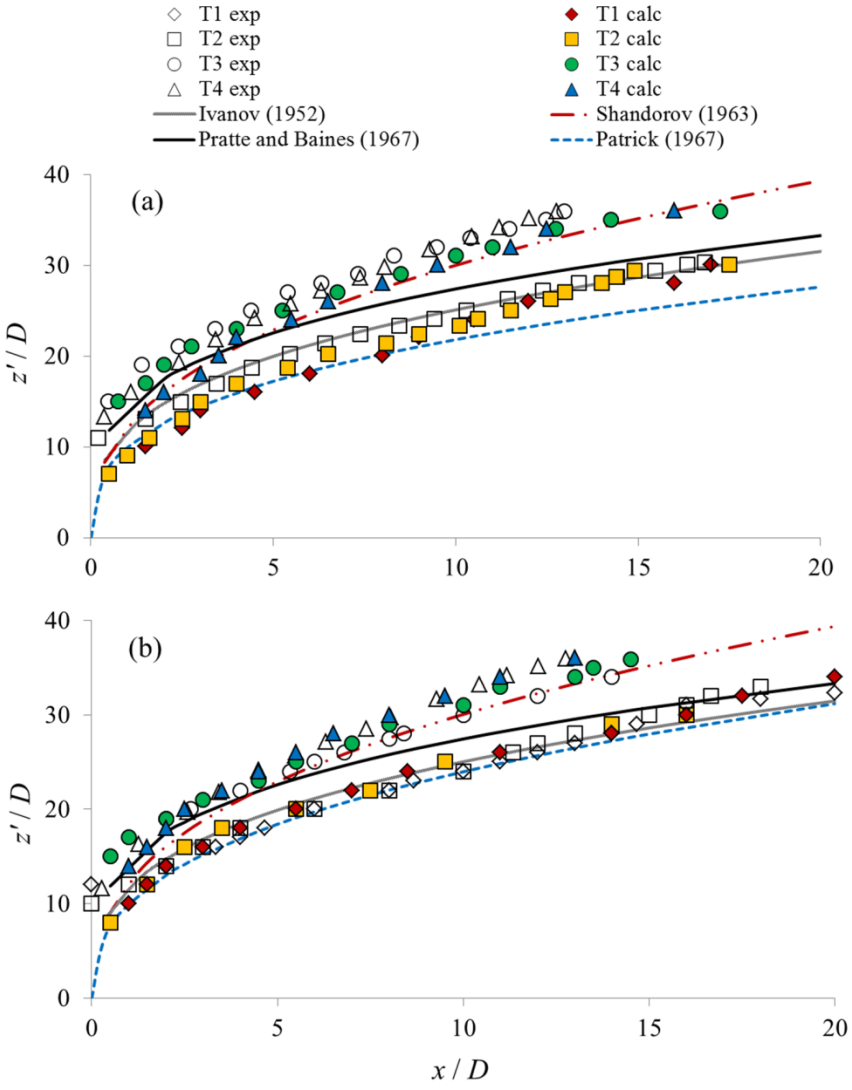

Figure 12 Centreline thermal jet trajectories obtained from analysis of (a) maximum temperatures T_m, and (b) maximum velocities U_m in experimental (exp) and numerical (calc) model results

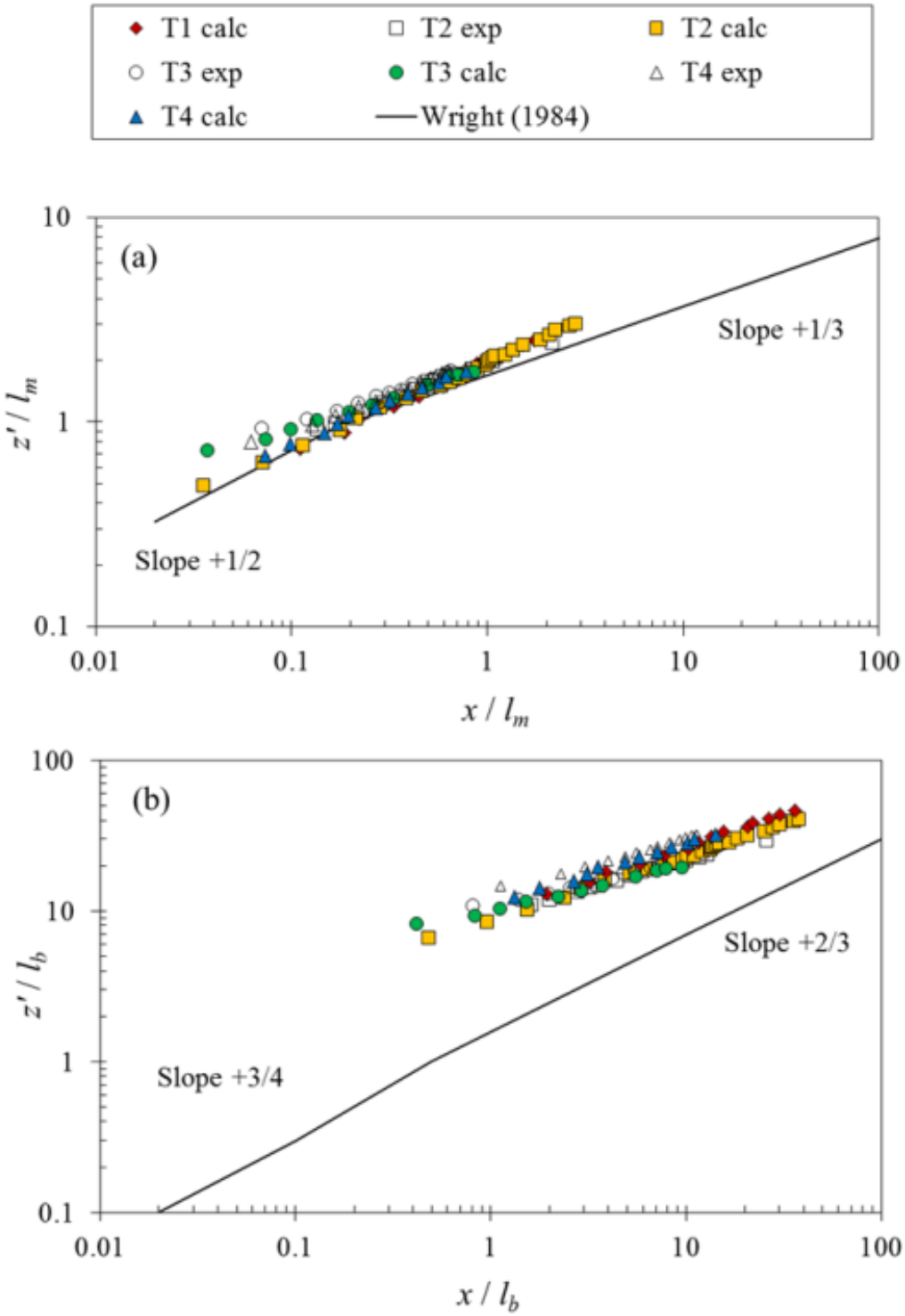

Figure 13 Scalar jet trajectories obtained by experiments and computations, with different scaling (a) l_m, (b) l_b. Comparison of data with integral model prediction by Wright (1984)